Bridging the Charge Accumulation and High Reaction Order for High-Rate Oxygen Evolution and Long Stable Zn-Air Batteries

Yawen Dai[1], Jie Yu[1,*], Jian Wang[1], Zongping Shao[2], Daqin Guan[1], Yu-Cheng Huang[3], Meng Ni[1,*]

[1]Department of Building and Real Estate, Research Institute for Sustainable Urban Development (RISUD), Research Institute for Smart Energy (RISE), The Hong Kong Polytechnic University, Hung Hom, Kowloon, Hong Kong, P. R. China.

[2]State Key Laboratory of Materials-Oriented Chemical Engineering, College of Chemical Engineering, Nanjing Tech University, No. 5 Xin Mofan Road, Nanjing 210009, P. R. China

[3]Department of Physics, Tamkang University, New Taipei City, Taiwan 25137, P. R. China

[*]Corresponding authors

E-mail addresses: yujie19920114@njtech.edu.cn (Jie Yu); meng.ni@polyu.edu.hk (Meng Ni)

Graphic abstract

Legend:
- Ir
- O
- Co

$$J=k[Q]^{\beta}$$

Co_3O_4 for high $[Q]$

Ir cluster for high β

Abstract

Combining noble metals with nonnoble metals is an attractive strategy to balance the activity and cost of electrocatalysts. However, a guiding principle for selecting suitable nonnoble metals is still lacking. Herein, we carry out a thorough mechanistic study on the platform oxygen evolution reaction (OER) electrocatalyst of Ir@Co$_3$O$_4$ to deeply understand the synergy between Ir and Co$_3$O$_4$ for the boosted OER. We demonstrate that the pseudocapacitive feature of Co$_3$O$_4$ plays the key role in accumulating sufficient positive charge ([Q]), while the Ir sites are responsible for achieving a high reaction order (β), synergistically contributing to the high OER activity of Ir@Co$_3$O$_4$ through the rate law equation. Specifically, Ir@Co$_3$O$_4$ displays a low overpotential of 280 mV at 10 mA cm^{-2} with a small Ir loading of 1.4 wt%. Ir@Co$_3$O$_4$ is further applied for Zn-air batteries, which enables the low charging potential and thus alleviates the oxidative corrosion of the air electrode, leading to improved cycle stability of 210 h at 20 mA cm^{-2}. This work demonstrates that anchoring active noble metal sites (for high β) on pseudocapacitive supports (for high [Q]) is highly favorable to the OER process, providing a clear guidance for boosting the utilization of noble metals in electrocatalysis.

Keywords: oxygen evolution, rate law analysis, pseudocapacitive, charge accumulation, reaction order

1. Introduction

To curb the carbon emission and meet the ever-increasing energy demand, innovative energy conversion technologies are urgently required to substitute fossil fuel combustion systems.[1,2] Oxygen evolution reaction (OER) plays a critical role in many electrochemical applications such as water splitting, carbon dioxide reduction, and rechargeable metal-air batteries.[3] However, the OER suffers from sluggish kinetics and the consequent large overpotentials, resulting in the low efficiency in various energy systems.[4]

The benchmark OER electrocatalysts (IrO_2, RuO_2) have noble metals and high costs, which impedes the practical application. Combining noble metals with nonnoble metals is an attractive strategy to balance the activity and cost. Researchers recently combined Ir and Ru species with nonnoble metal oxides and hydroxides by doping or surface anchoring to realize high activity with low noble metal dosage.[5-8] For instance, Ir was doped into the perovskite structure to get $SrZr_xIr_{1-x}O_3$, achieving the improved OER activity (1.47 V vs. RHE at 10 mA cm^{-2}) with decreased Ir content (40 wt%) as compared to IrO_2.[8] Loading atomic Ir on NiO realized 1.445 V vs. RHE at 10 mA cm^{-2} for OER with the low Ir content of 18 wt%.[9] Lu et al. decorated ultrasmall RuO_x clusters on Co_3O_4 with a Ru ratio of 4.4 wt%, which delivered OER performance of 1.51 V vs. RHE at 10 mA cm^{-2}.[10] However, the standard of selecting the non-precious metal substrate is unclear, and the mechanism behind the synergistic effects of hybridizing noble metals and non-noble supports remains elusive. An in-depth study is thus required to tackle those issues and provide guidance for rationally designing such hybrid catalysts.

Previous studies on OER can be consulted to derive important clues for the synergy.[11-14] Since OER is a multielectron transfer process, multiple charges should be accumulated to drive the chemical bond formation.[15] Shao-Horn's group reveals that the OER activity scales with the charge storage capacity of the electrocatalysts, and thus they suggest that the accumulated charge corresponds to the generation of surface reaction sites.[16,17] Moreover, the physical origin of the charge accumulation was studied, demonstrating that the high-valent metal centers and the deprotonated absorbates are responsible for the positive charge storage on the electrocatalyst surface, and it confirms the key role of positive charge accumulation on the OER activity.[16,18,19] In addition to charge accumulation, a high reaction order with respect to the surface charge is also significant to drive the high-rate OER.[20,21] The rate law equation $J=k[Q]^\beta$ (k stands for the reaction constant) describes the relationship between the reaction rate (J), the catalyst accumulated charge (Q), and the reaction order (β), and it has been successfully

4

applied in interpreting photochemical OER processes.[22-25] However, few studies have ever applied the rate law equation to understand electrocatalytic OER systems.

Inspired by the above findings, we carry out a mechanistic study based on the rate law equation, aiming to construct a guiding principle for designing noble metal-nonnoble metal hybrid OER electrocatalysts. Specifically, highly dispersed Ir species anchored on Co_3O_4 ($Ir@Co_3O_4$) is used as a model catalyst due to the promising activity and stability.[26] Through detailed electrochemical analysis and theoretical calculation, we demonstrate that Co_3O_4 contributes to the high charge accumulation with the outstanding pseudocapacitive behavior, and Ir sites are responsible for the high reaction order due to the high intrinsic kinetics. Resultantly, high OER activity is achieved with a particularly low Ir loading of only ~1.4 wt%. The prepared $Ir@Co_3O_4$ requires a low overpotential of 280 mV vs. RHE at 10 mA cm^{-2} in 0.1 M KOH and sustains a long stability of 120 h, outperforming the bare Co_3O_4 and benchmark IrO_2. Furthermore, a rechargeable Zn-air battery (ZAB) using $Ir@Co_3O_4$ as the air electrode enables a low charging potential of 2.04 V at 40 mA cm^{-2} and can be stably cycled at 20 mA cm^{-2} for 210 h. In addition to reporting a high-performance OER electrocatalyst, this work contributes to guiding the rational design of a large family of hybrid catalysts by combining intrinsically active noble metal sites with pseudocapacitive nonnoble metal supports.

2. Result and Discussion

2.1 Crystal structure, morphology, and chemical composition

$Ir@Co_3O_4$ is synthesized by a very simple stirring treatment of $CoCO_3$ powder in $IrCl_4$ solution followed by low-temperature calcination, and the detailed process is described in supporting information (**Figure S1**), which is especially suitable for mass production. The X-ray diffraction (XRD) patterns (**Figure S2**) show that the $Ir@Co_3O_4$ preserves the crystal structure of spinel Co_3O_4. Relative to the pristine sample, the Ir decoration induced the left shift of the peaks, which evidences the elongated Co-O bonds due to electronic interaction between

5

Ir sites and Co_3O_4. As shown in **Figure 1a,** the red-shifted peaks of the Raman spectrum in $Ir@Co_3O_4$ are also observed as compared to the bare Co_3O_4, corresponding to the XRD results. Besides, no XRD or Raman signals corresponding to IrO_2 or Ir metals are observed in $Ir@Co_3O_4$, possibly due to their low mass loading and high dispersion. The scanning electron microscopy (SEM) (**Figure S3a**) shows the randomly aggregated $Ir@Co_3O_4$ particles with no featured morphology. Transmission electron microscopy (TEM) images (**Figure S3b**) show the small crystal size around 10~20 nm. The Brunauer−Emmett−Teller (BET) method (**Figure S4**) renders the specific surface area of 37.1 g cm^{-2} of the $Ir@Co_3O_4$. In the high-resolution TEM (HRTEM) image (**Figure 1b**) the lattice fringes with d-spacing of 0.244 nm corresponding to (311) plane and 0.285 nm corresponding to (220) plane can be clearly identified. In the high-angle annular dark-field scanning transmission electron microscopy (HAADF-STEM) image (**Figure 1c**), Ir species can be recognized as bright sub-nanometer clusters, confirming atom-scale dispersion. The mass content of Ir is determined to be 1.4 wt% by inductively coupled plasma atomic emission spectrometry. The large-area HAADF-STEM image (**Figure 1d**), X-ray energy dispersive (EDX) spectrum (**Figure S5**), and mapping images (**Figure 1e-1f**) are collected, demonstrating that Ir sites are distributed on the entire Co_3O_4 support.

Furthermore, soft X-ray absorption spectroscopy (XAS) and hard XAS [including X-ray absorption near-edge structure (XANES) and extended X-ray absorption fine structure (EXAFS)] are analyzed to reveal the electronic structure and local structure of materials.[27] For soft XAS of O-K edge (**Figure 1g**), IrO_2 shows the lowest pre-edge peak energy among three samples, corresponding to the highest metal-oxygen covalency among three samples. As compared to the bare Co_3O_4, $Ir@Co_3O_4$ shows almost similar O-K edge spectra, indicating that the O electronic structure of $Ir@Co_3O_4$ is dominated by the Co_3O_4 component.[28] For soft XAS of Co L_3 edge (**Figure 1h**), $Ir@Co_3O_4$ exhibits almost the same spectral feature as compared to the bare Co_3O_4, implying their similar Co electronic structures. Besides, for the XANES spectra of Ir-L_3 edge (**Figure 1i**), the while line feature of $Ir@Co_3O_4$ is very close to that of Ir

foil, suggesting that the Ir species in Ir@Co_3O_4 sample dominantly has a metallic feature. In the Fourier transformed (FT)-EXAFS spectra of Ir-L_3 edge **(Figure 1j, Figure S6, Table S1)**, Ir@Co_3O_4 shows a major Ir-Ir/Co shell peak which is similar with the Ir foil, further validating the metallic Ir for Ir@Co_3O_4. Combining the electronic states and coordination environment of Ir and Co in our samples, we can conclude that the chemical nature of Ir species is metallic Ir clusters anchored on Co_3O_4.
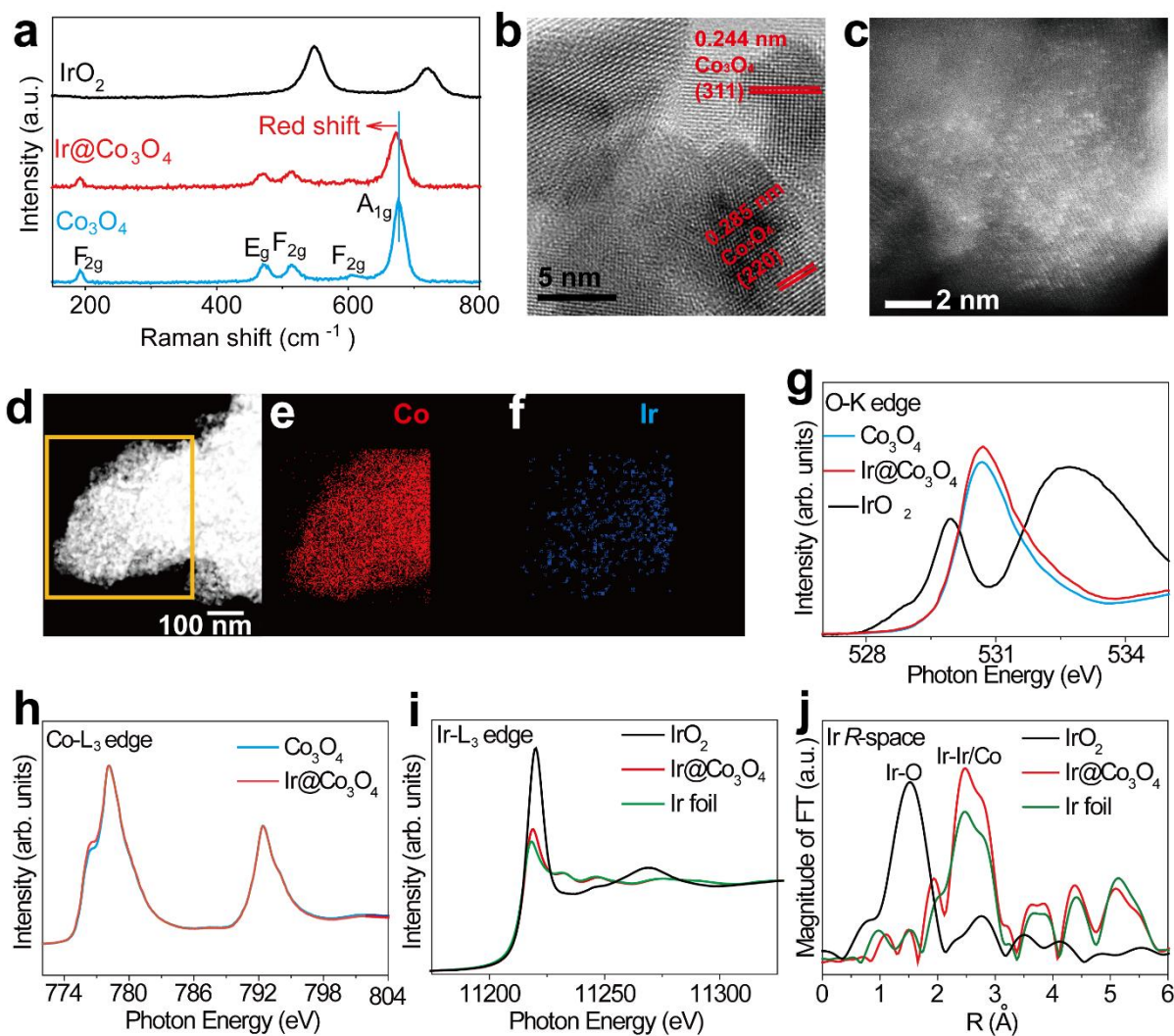
Figure 1 (a) Raman spectra of bare Co_3O_4, Ir@Co_3O_4, and IrO_2. (b) HRTEM image and (c) High-resolution HADDF-STEM image of Ir@Co_3O_4. (d) Large-scale HADDF-STEM image and the corresponding EDX-mapping image of (e) Co and (f) Ir. (g) Soft XAS spectrum of O-K edge. (h) Soft XAS spectrum of Co-L_3 edge. (i) XANES spectra of Ir-L_3 edge. (j) FT-EXAFS spectra of Ir-L_3 edge.

2.2　Electrochemical activity and mechanism study

In the OER linear scan voltammetry (LSV) curves (**Figure 2a**), Ir@Co$_3$O$_4$ displays a low potential of 1.51 V vs. RHE at 10 mA cm^{-2} (E$_{j=10\,mA\,cm-2}$), which is smaller than the bare Co$_3$O$_4$ (1.60 V vs. RHE) and IrO$_2$ (1.56 V vs. RHE), demonstrating the superior OER activity of Ir@Co$_3$O$_4$. The OER activity of the Ir@Co$_3$O$_4$ outperforms most of the recently reported metal-metal oxide hybrid electrocatalysts as shown in **Table S2**. Furthermore, the mass activity (MA) is calculated at the overpotential (η) of 300 mV (**Figure 2b**), and Ir@Co$_3$O$_4$ shows higher MA (32.2 A g$_{Ir@Co_3O_4}$ $^{-1}$) than the bare Co$_3$O$_4$ (MA=1.8 A g$_{Co_3O_4}$ $^{-1}$,) and IrO$_2$ (MA=11.8 A g$_{IrO_2}$ $^{-1}$). The electrochemically active surface area (ECSA) is evaluated by the double-layer capacitance (C$_{dl}$) tests (**Figure S7**). C$_{dl}$ is calculated to be 34.9 mF cm^{-2} for Co$_3$O$_4$, 31.5 for Ir@Co$_3$O$_4$, and 28.3 mF cm^{-2} for IrO$_2$. The ECSA-normalized specific activity (SA) at η=300 mV is shown in **Figure 2b**. Ir@Co$_3$O$_4$ (SA=20.5 μA cm^{-2}) offers higher specific activity than the bare Co$_3$O$_4$ (SA=1.0 μA cm^{-2}) and IrO$_2$ (SA=8.3 μA cm^{-2}), demonstrating the effectiveness of the hybrid strategy. In the Nyquist plots of electrochemical impedance spectra (EIS) displayed in **Figure S8,** Ir@Co$_3$O$_4$ shows decreased interfacial charge transfer resistance in comparison to Co$_3$O$_4$ and IrO$_2$, at both 1.53 V vs. RHE and the open circuit potential, which can be attributed to the metallic nature of Ir cluster in Ir@Co$_3$O$_4$ as suggested by FT-EXAFS (**Figure 1j**). Ir@Co$_3$O$_4$ also shows a better stability than the bare Co$_3$O$_4$ and IrO$_2$ (**Figure 2c**). The Ir@Co$_3$O$_4$/carbon paper electrode can be stably performed at 10 mA cm^{-2} for 120 h with a small potential increase of 0.067 V (**Figure 2d**).

The samples after the chronopotentiometry test were characterized. The X-ray photoelectron spectra (XPS) (**Figure S9**) indicates the increased valence state of Co and Ir after the electrochemical test, which is common for OER catalysts. The XRD pattern (**Figure S10**) shows that the post-OER Ir@Co$_3$O$_4$ still preserves the original crystal structure of spinel cobalt oxide, indicating the good structural stability of Ir@Co$_3$O$_4$ during OER. Moreover, the HRTEM images of the post-OER samples (**Figure S11**) imply that the Ir clusters on Ir@Co$_3$O$_4$ can

8

decrease the amorphization of Co_3O_4 under the alkaline OER condition, which might be an important reason for the enhanced long-term stability of $Ir@Co_3O_4$ as compared to the bare Co_3O_4.
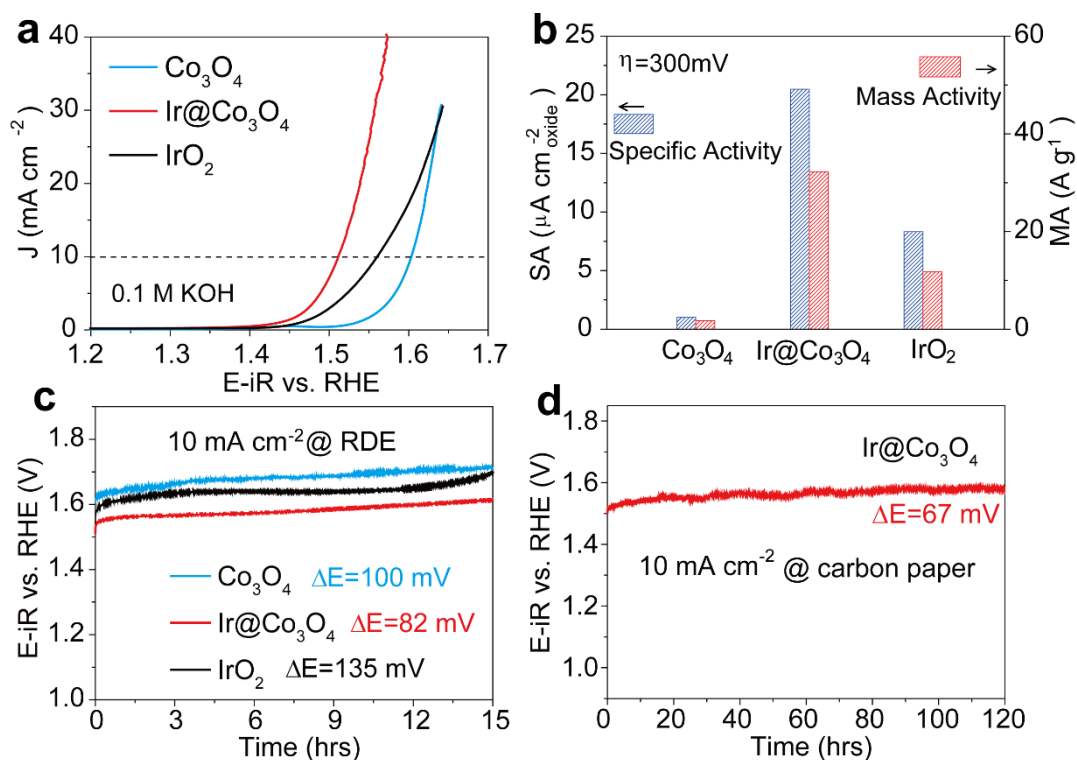

Figure 2. (a) OER-LSV curves of Co_3O_4, $Ir@Co_3O_4$, and IrO_2. (b) The corresponding specific activity and mass activity of OER at the overpotential of 300 mV. (c) Chronopotentiometry response of OER durability of three samples on RDE at 10 mA cm^{-2} and (d) $Ir@Co_3O_4$ on carbon paper. The loading mass is fixed at 0.5 mg$_{cat}$ cm^{-2} for RDE test and 2 mg$_{cat}$ cm^{-2} for carbon paper test. The potential values are iR-corrected.

Thereafter, the charge accumulation property and the reaction order of the three samples are investigated to get the in-depth understanding of the synergy between Ir sites and Co_3O_4 supports. In the cyclic voltammetry curves (**Figure 3a**), Co_3O_4 exhibits the featured redox peak of Co (II/III) and Co (III/IV), which is typical for the pseudocapacitive charge accumulation. In comparison to Co_3O_4, $Ir@Co_3O_4$ shows negatively shifted Co redox peaks, as well as the suppressed cathodic peak concomitantly with the lowered onset potential of OER. The change of peak position and peak area indicates the smooth charge transfer from Co_3O_4 to Ir sites in

9

the hybrid Ir@Co_3O_4.[29,30] Pulse voltammetry is used to quantify the accumulated positive charge on electrocatalysts.[19,31] The electrocatalyst is initially set at the aimed positive potential and then abruptly switched to the open circuit potential (OCP) (**Figure 3b, Figure S12**), and the cathodic transient current peak is integrated to determine the accumulated positive charge (Q). The relationship between Q, OER current density (J), and the applied potential (E) are summarized in **Figure 3c**. Co_3O_4, Ir@Co_3O_4, and IrO_2 exhibit very similar shapes of Q-E curves and J-E curves. All the curves show two distinct features in two potential regions, and the two regions can be distinguished by the OER onset potential. Before the onset potential, negligible OER current is observed, and the electrocatalysts display a capacitor-like behavior as indicated by the linear relation between the Q and E. After the onset potential, OER current starts to grow, whereas the accumulated charge preserves a constant value with further increased positive applied potential. The observation demonstrates that the electrocatalysts should accumulate a critical number of positive charges to trigger the OER reaction.

The charge storage capacity of the three electrocatalysts can be assessed from the slope of ($\partial Q/\partial E$) in the linear region, giving the capacitance value of 131 mF cm^{-2} for Co_3O_4, 83.1 mF cm^{-2} for Ir@Co_3O_4, and 29.2 mF cm^{-2} for IrO_2. Moreover, the double-layer capacitance (C_{dl}) (**Figure S7**) is subtracted from the C($\partial Q/\partial E$) to calculate the pseudocapacitive contribution (C_{pseudo}) of Co_3O_4 (96.1 mF cm^{-2}), Ir@Co_3O_4 (51.6 mF cm^{-2}), and IrO_2 (0.9 mF cm^{-2}). As summarized in **Figure 3d**, the charge accumulation of Co sites is mainly contributed by C_{pseudo}, while that of Ir sites is mainly contributed by C_{dl}. The reason might be due to the different potential regions of Co redox and Ir redox. Although IrO_2 has pseudocapacitive feature through the redox behavior of Ir(III/IV/V), the potential region is around 0.4~1.0 V vs. RHE (**Figure S13**), which is far from the onset of OER (~1.5 V vs. RHE). In contrast, the Co (III/IV) redox is at the potential region of 1.4~1.5 V vs. RHE that is close to the OER onset. Moreover, IrO_2 shows the rectangular CV shape at 1.4~1.5 V vs. RHE, indicating the double-layer capacitive feature (**Figure S13**). We hence conclude that, for achieving large charge accumulation

10

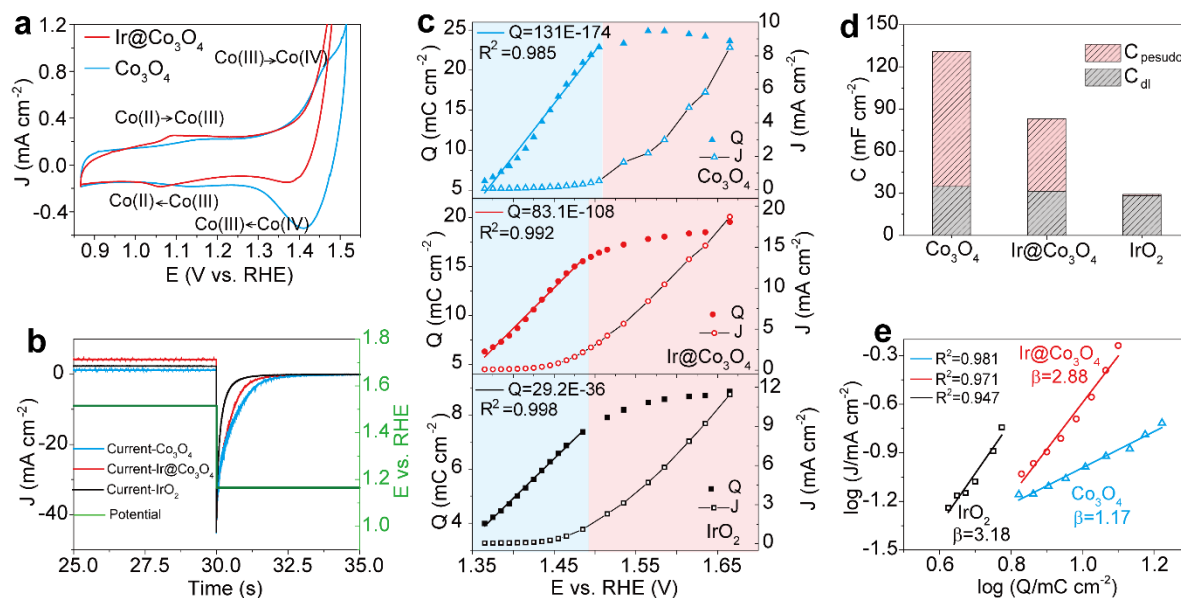capacity utilized for OER, the material should have pseudocapacitive feature close to the OER potential.

Figure 3. (a) CV curves within the Co redox potential range at the scan rate of 5 mV s^{-1} in 0.1 M KOH. (b) Representative pulse voltammetry protocol showing the oxidative potenital-OCP step and the corresponding pulse current response. (c) Q~E and J~E plots calculated from the pulse voltammetry form Figure S8. (d) Comparison of the pesudocapacitance and double layer capacitance. (e) Log (J) versus log (Q) and the linear fitting for the calculation of reaction order of Co_3O_4, $Ir@Co_3O_4$, and IrO_2. All the potential values are non iR corrected.

To scrutinize how the charge accumulation triggers the OER current, we carry out the rate law analysis (**Figure 3e**). The quantitative correlation between charge accumulation and the reaction rate of electrocatalytic OER can be described by the rate law equation, $J=k[Q]^{\beta}$, where k is the rate constant, $[Q]$ stands for the density of the accumulated positive charge, and β is the reaction order.[20] To singly reveal the intrinsic kinetics and eliminate the impact of mass transfer and bubble growth under large current density condition,[32,33] the rate law analysis is carried out at low current density within the narrow potential region close to the onset potential of each sample. The log(J)~log(Q) curves of the three samples show linear features around OER onset potential (**Figure 3e, Figure S14**). Accordingly, the β values are extracted from the

11

fitted slopes of the log(J)~log(Q) curves. The reaction order grows higher with the increased Ir content following the tendency of IrO_2 (β=3.18)>$Ir@Co_3O_4$ (β=2.88)>Co_3O_4 (β=1.17), validating that the Ir sites play the key role in achieving a high reaction order. Combining the above results, the insights of promoted OER by the hybrid strategy are clarified. The Co_3O_4 support contributes to the large charge accumulation, and Ir sites boost the high reaction order, and the two features synergistically lead to the fast OER rate of $Ir@Co_3O_4$.

Furthermore, we demonstrate that the high reaction order of Ir sites comes from the high intrinsic OER kinetics. Tafel slopes are displayed in **Figure 4a**. To eliminate the interruption of the capacitive current of Co redox on the Tafel slopes, the data points are acquired by chronoamperometry tests at a series of potential values (**Figure S15**) instead of extracting from the LSV curves. Co_3O_4, $Ir@Co_3O_4$, and IrO_2 show the Tafel slope of 126, 73, and 69 mV dec^{-1}, implying the intrinsic reaction kinetics in the order of IrO_2>$Ir@Co_3O_4$>Co_3O_4. As a complementary evidence, the peak frequency of EIS-Bold plot (**Figure 4b**) is measured to reflect the time scale for interfacial charge transfer.[34] The Bode plots deliver a tendency of IrO_2 (1.26 Hz) > $Ir@Co_3O_4$ (1 Hz) > Co_3O_4 (0.25 Hz), agreeing well with the Tafel slopes. Furthermore, the structure models (**Figure 4c**, **Figure S16**) for DFT calculation were constructed based on the characterization (**Figure 1**) and the conventional adsorbate evolution mechanism (AEM) of OER.[35] The density of function (DOS) results (**Figure 4d**) show that $Ir@Co_3O_4$ has zero band gap, and it has higher DOS than the bare Co_3O_4 around the fermi level, indicating the metallic nature and the superior electron transport property of $Ir@Co_3O_4$.[36] The Gibbs free-energy diagram (**Figure 4e**) shows the OER energy barrier in order of IrO_2 (0.40 eV) < Ir site of $Ir@Co_3O_4$ (0.48 eV) < Co site of $Ir@Co_3O_4$ (0.61 eV) <Co_3O_4 (0.72 eV). Considering the in-situ oxidation of Ir and Co during OER (**Figure S**9) and the possible reconstruction of the catalyst surface,[37] the calculation is conducted on the IrO_2/CoOOH model (**Figure S17-S18**) as a complement, and the consistent tendency is obtained. The tendency of the DFT-calculated OER energy barrier agree well with the Tafel slopes and EIS-Bode plots,

12

as well as the previous reports clarifying the high intrinsic OER kinetics of Ir sites.[38-40] The consistent tendency between the β value and the DFT-calculated energy barrier proves that the high reaction order of Ir sites is due to the high intrinsic OER kinetics.
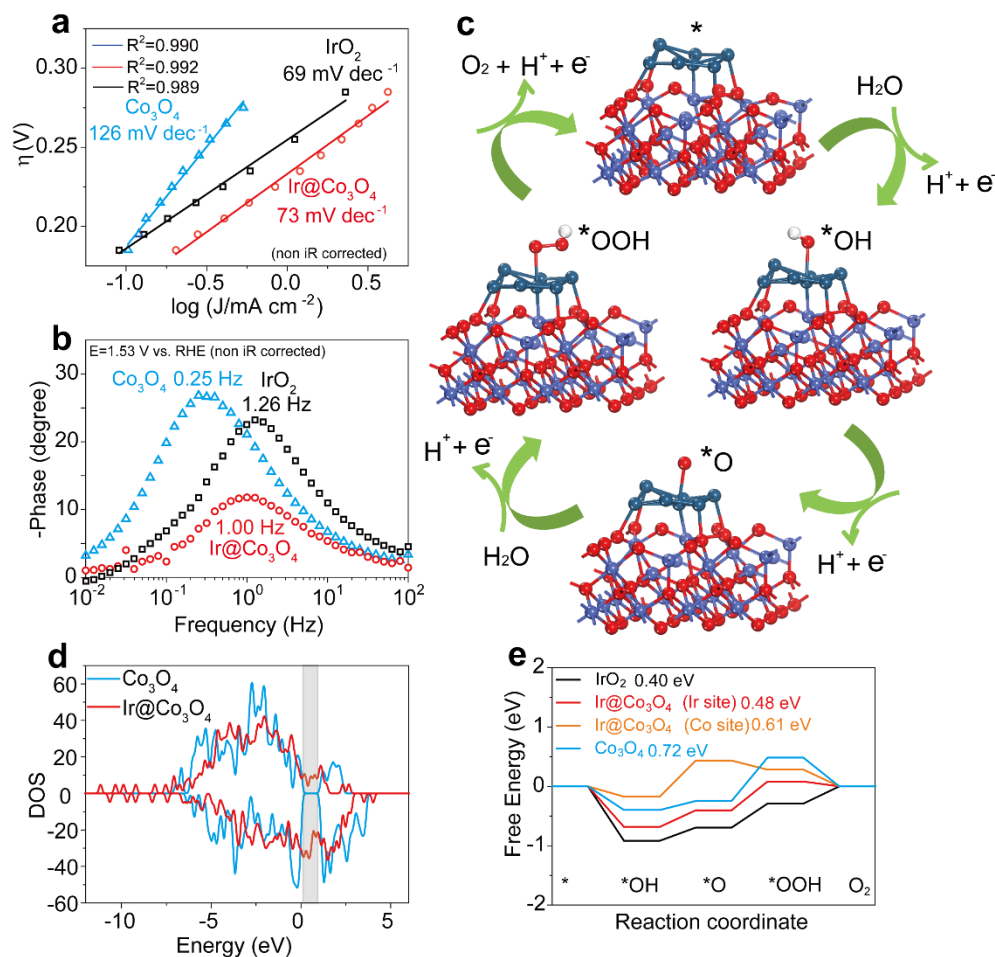

Figure 4. (a) OER-Tafel slopes and (b) EIS-Bode plots at 1.53 V vs. RHE of Co_3O_4, $Ir@Co_3O_4$, and IrO_2. (c) Structure of $Ir@Co_3O_4$ and the OER intermediates adsorbed on the Ir site. The blue, purple, red, white balls represent Ir, Co, O, and H atoms, respectively. (d) DOS of Co_3O_4 and $Ir@Co_3O_4$. (e) Gibbs free-energy diagram for the OER four steps on the Co site of Co_3O_4, the Ir site of IrO_2, the Co and Ir sites of $Ir@Co_3O_4$ calculated at U=1.23 V. All the potential values are non iR corrected.

2.3 Application in fast charging Zn-air batteries

After the strategy demonstration of the OER electrocatalyst design, we consider the device application of $Ir@Co_3O_4$. The unique advantage of high-rate OER can be utilized for the fast

13

charging of ZABs, which is quite important for the practical application.[41,42] Oxygen reduction reaction (ORR) activity is assessed to guarantee the discharge performance of ZABs. In the LSV curves (**Figure 5a**, **Figure S19a**), Ir@Co_3O_4 delivers ORR half-wave potential ($E_{1/2}$) of 0.75 V vs. RHE, which is significantly more active than the bare Co_3O_4 with $E_{1/2}$=0.56 V vs. RHE. The improved ORR activity of Ir@Co_3O_4 can be ascribed to the stronger O_2 adsorption as reflected by the open circuit potential difference in O_2 and N_2 saturated electrolyte (**Figure S19b**).[13,43] The ORR electron transfer number is calculated to be 3.52 for Ir@Co_3O_4 and 3.98 for the benchmark Pt/C (**Figure S20**). Moreover, Ir@Co_3O_4 persists a stable ORR chronoamperometry response with 88 % current retention at 0.3 V vs. RHE for 17 h (**Figure 5b**), similar with Pt/C, indicating the good long-term durability. The bifunctional activity is evaluated by the potential gap (ΔE) between $E_{j=10}$ of OER and $E_{1/2}$ of ORR (**Figure 5c**). Ir@Co_3O_4 displays a ΔE of 0.76 V, which is comparable to the benchmark Pt/C+IrO_2 (0.71 V) and significantly lower than that of bare Co_3O_4 (1.04 V), showing the good potential of application in ZABs. Using the cell configuration of **Figure S21** for ZAB assembling, Ir@Co_3O_4 delivers the peak power density of 163 mW cm^{-2}, which is close to Pt/C+IrO_2 (194 mW cm^{-2}) (**Figure S22a**). When operated as primary batteries (**Figure S22b**), the Ir@Co_3O_4 assembled ZAB and the Pt/C+IrO_2 assembled ZAB displayed the specific capacity of 712 mAh g^{-1}_{Zn} and 675 mAh g^{-1}_{Zn}, respectively.

The fast-charging performance of ZABs is evaluated by galvanostatic charge/discharge test at a fixed areal capacity of 30 mAh cm^{-2}/cycle (**Figure 5d**). Ir@Co_3O_4 displays charging potential of 1.95 V, 1.98 V, 2.02 V, and 2.04 V when charging at 10, 20, 30, and 40 mA cm^{-2}, respectively, and it also shows a stably retained discharge voltage of 1.15 V at 10 mA cm^{-2} after the whole fast-charging test of 54 h. In comparison, Pt/C+IrO_2 couple shows much higher charging voltage of 2.00 and 2.06 at 10 and 20 mA cm^{-2}. More notably, Pt/C+IrO_2 shows a rapid increasement of charging voltage from 2.14 V to 2.41 V at the second cycle of 30 mA cm^{-2} charging, which leads to the serious oxidative degradation of air electrode, and thus

14

resulting in the significantly decreased discharge voltage of 0.86 V at 10 mA cm^{-2} after the fast-charging performance test. **Figure 5e** shows the energy efficiencies of ZABs with fixed areal capacity of 30 mAh cm^{-2}/cycle at different charging rate. When performed at the gradually increased charging rate with the charging time/discharging time from 1/1 to 1/4, Ir@Co$_3$O$_4$ delivers slightly decreased energy efficiency from 62% to 57%, whereas Pt/C+IrO$_2$ exhibits dramatically decreased energy efficiency of from 64% to 35%. Moreover, the Ir@Co$_3$O$_4$ assembled ZAB shows stable cycle profiles of for over 720 cycles with sustained energy efficiency of 58% when performed at 10 mA cm^{-2} and 20 min/cycle, which is significantly more stable than Pt/C+IrO$_2$ with the energy efficiency decayed to 50 % in 300 cycles (**Figure 5f and 5g**). The Ir@Co$_3$O$_4$ assembled ZAB is further cycled at a large capacity[44] at the condition of 20 mA cm^{-2} and 3 h/cycle, and the Ir@Co$_3$O$_4$ preserves the original crystal structure at both charged and discharged states (**Figure S23**). The ZAB can be stably performed for 70 cycles (210 h) with the preserved energy efficiency of 52.7% (**Figure S24**). The above results demonstrate that Ir@Co$_3$O$_4$ is a rather promising material for the fast charging and long stable ZABs.

The superior cycle stability of Ir@Co$_3$O$_4$ assembled ZAB can be attributed to the good OER activity and the resultant low charging potential, which effectively alleviates the oxidative corrosion of air electrodes. Ex-situ characterization was carried out for the Pt/C+IrO$_2$ and Ir@Co$_3$O$_4$ air electrodes after the battery cycling at 20 mA cm^{-2} and 3 h/cycle for 15 cycles (**Figure S25a**). The post-cycling electrolyte of Pt/C+IrO$_2$ showed dark brown color due to the severe carbon carrion whereas that of the Ir@Co$_3$O$_4$ showed light yellow color due to the decreased carbon (**Figure S25b**). In addition, the optical photos (**Figure S25c-f**) and the SEM images (**Figure S26**) show that the Pt/C+IrO$_2$ air electrode evolves seriously cracked surface after cycling, whereas the Ir@Co$_3$O$_4$ air electrode preserves the original flat surface. Moreover, in the Raman spectra (**Figure S25g**), the Pt/C+IrO$_2$ air electrode exhibits significantly decreased carbon signal after cycling, indicating the severe carbon corrosion, while the

15

Ir@Co$_3$O$_4$ air electrode shows unchanged peak intensity of carbon component. The above results highlight the key role of the good OER activity in enhancing the cycle stability of air electrodes.
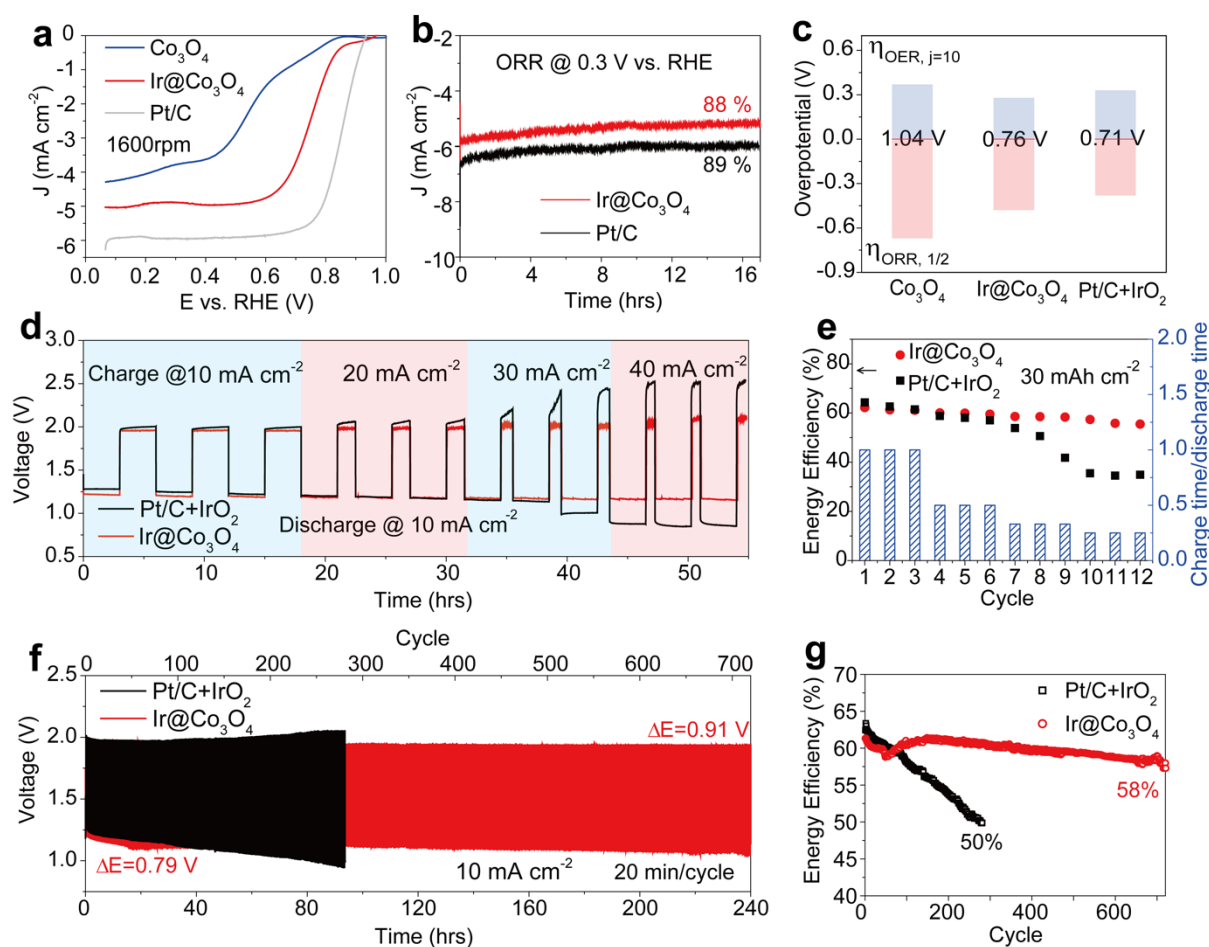
Figure 5. (a) ORR-LSV curves of Co$_3$O$_4$, Ir@Co$_3$O$_4$, and Pt/C. The background current density has been deducted (Figure S19). (b) ORR durability tested by chronoamperometry response of Ir@Co$_3$O$_4$ and Pt/C at 0.30 V vs. RHE. (c) Potential gaps of Co$_3$O$_4$, Ir@Co$_3$O$_4$, and Pt/C+IrO$_2$ between E$_{1/2}$ of ORR and E$_{j=10}$ of OER.The loading mass for RDE test is fixed at 0.5 mg$_{cat}$ cm^{-2}. Fast-charging performance test of of Ir@Co$_3$O$_4$ and Pt/C+IrO$_2$ tested with a fixed areal capacity of 30 mAh cm^{-2}/cycle at different charge densities from 10 to 40 mA cm^{-2} and fixed discharge current density of 10 mA cm^{-2}: (d) galvanostatic V-t profiles and (e) the corresponding energy efficiency and charge/discharge time ratio. (f) Cycle stability of Ir@Co$_3$O$_4$ and Pt/C+IrO$_2$ assembled ZABs tested at 10 mA cm^{-2} and 20 min/cycle and (g) the corresponding energy efficiency. The loading mass for battery test is fixed at 2 mg$_{cat}$ cm^{-2}.

16

3. Conclusions

In summary, by using Ir@Co_3O_4 as the model catalyst, we reveal the unique contributions nonnoble substrate and supported noble metals, clarifying the synergy mechanism in realizing high-rate OER. The Ir@Co_3O_4 has strong interfacial electronic coupling, efficient interfacial charge transfer, and it also realizes high utilization of the noble metal. Ir@Co_3O_4 displays the low OER overpotential of 280 mV at 10 mA cm^{-2} with a low Ir loading of 1.4 wt%. An insightful rate law analysis and theoretical calculation validate that the Co_3O_4 is responsible for the abundant charge accumulation due to the pseudocapacitive feature, while Ir sites play the key role in achieving the high reaction order due to the high intrinsic kinetics. The synergy of the two features delivers the high OER rate and enables the potential application of Ir@Co_3O_4 as a high-performance OER catalyst as demonstrated by the ZABs. Specifically, Ir@Co_3O_4 achieved a low charging potential of 2.04 V at 40 mA cm^{-2} during ZAB application, and it can be stably operated for 210 h at 20 mA cm^{-2}. This work reveals the different roles of noble metals and nonnoble metals and the synergy mechanism during OER electrocatalysis, highlighting the significance of pseudocapacitive property in selecting suitable nonnoble metal supports and providing guidance for future electrocatalyst development.

Supporting Information

Supporting Information is available from the Wiley Online Library or from the author.

Acknowledgements

17

Declaration of competing interests

The authors declare no conflict of interests.

References

[1]   Song, J.; Wei, C.; Huang, Z.-F.; Liu, C.; Zeng, L.; Wang, X.; Xu, Z. J., A review on fundamentals for designing oxygen evolution electrocatalysts. *Chem. Soc. Rev.* **2020,** *49* (7), 2196-2214.

[2]   Yang, H.; Han, X.; Douka, A. I.; Huang, L.; Gong, L.; Xia, C.; Park, H. S.; Xia, B. Y., Advanced oxygen electrocatalysis in energy conversion and storage. *Adv. Funct. Mater.* **2021,** *31* (12), 2007602.

[3]   Yu, J.; Ran, R.; Zhong, Y.; Zhou, W.; Ni, M.; Shao, Z., Advances in porous perovskites: synthesis and electrocatalytic performance in fuel cells and metal–air batteries. *Energy Environ, Mater,* **2020,** *3* (2), 121-145.

[4]   Zhang, J.; Cui, J.; Eslava, S., Oxygen Evolution Catalysts at Transition Metal Oxide Photoanodes: Their Differing Roles for Solar Water Splitting. *Adv. Energy Mater.* **2021,** *11* (13), 2003111.

[5]   Xiao, M.; Zhu, J.; Li, S.; Li, G.; Liu, W.; Deng, Y.-P.; Bai, Z.; Ma, L.; Feng, M.; Wu, T., 3d-Orbital occupancy regulated Ir-Co atomic pair toward superior bifunctional oxygen electrocatalysis. *ACS Catal.* **2021,** *11* (14), 8837-8846.

[6]   Shi, Z.; Wang, Y.; Li, J.; Wang, X.; Wang, Y.; Li, Y.; Xu, W.; Jiang, Z.; Liu, C.; Xing, W., Confined Ir single sites with triggered lattice oxygen redox: Toward boosted and sustained water oxidation catalysis. *Joule* **2021,** *5* (8), 2164-2176.

[7]   Yin, J.; Jin, J.; Lu, M.; Huang, B.; Zhang, H.; Peng, Y.; Xi, P.; Yan, C.-H., Iridium single atoms coupling with oxygen vacancies boosts oxygen evolution reaction in acid media. *J. Am. Chem. Soc.* **2020,** *142* (43), 18378-18386.

[8]   Liang, X.; Shi, L.; Cao, R.; Wan, G.; Yan, W.; Chen, H.; Liu, Y.; Zou, X., Perovskite-Type Solid Solution Nano-Electrocatalysts Enable Simultaneously Enhanced Activity and Stability for Oxygen Evolution. *Adv. Mater.* **2020,** *32* (34), 2001430.

[9]   Wang, Q.; Huang, X.; Zhao, Z. L.; Wang, M.; Xiang, B.; Li, J.; Feng, Z.; Xu, H.; Gu, M., Ultrahigh-loading of Ir single atoms on NiO matrix to dramatically enhance oxygen evolution reaction. *J. Am. Chem. Soc.* **2020,** *142* (16), 7425-7433.

[10]   Lu, Q.; Guo, Y.; Mao, P.; Liao, K.; Zou, X.; Dai, J.; Tan, P.; Ran, R.; Zhou, W.; Ni, M., Rich atomic interfaces between sub-1 nm RuO_x clusters and porous Co_3O_4 nanosheets boost oxygen electrocatalysis bifunctionality for advanced Zn-air batteries. *Energy Stor. Mater.* **2020,** *32*, 20-29.

[11]   Yang, X.; Wang, Y.; Li, C. M.; Wang, D., Mechanisms of water oxidation on heterogeneous catalyst surfaces. *Nano Research* **2021**, 1-12.

[12]   Exner, K. S., Recent progress in the development of screening methods to identify electrode materials for the oxygen evolution reaction. *Adv. Funct. Mater.* **2020,** *30* (42), 2005060.

[13]   Ede, S. R.; Luo, Z., Tuning intrinsic catalytic activities of oxygen-evolution catalysts by doping: a comprehensive review. *J. Mater. Chem. A* **2021**.

[14]   Dai, Y.; Yu, J.; Cheng, C.; Tan, P.; Ni, M., Mini-review of perovskite oxides as oxygen electrocatalysts for rechargeable zinc–air batteries. *Chem. Eng. J.* **2020,** *397*, 125516.

[15]   Ooka, H.; Yamaguchi, A.; Takashima, T.; Hashimoto, K.; Nakamura, R., Efficiency of oxygen evolution on iridium oxide determined from the pH dependence of charge accumulation. *J. Phys. Chem. C* **2017,** *121* (33), 17873-17881.

[16]   Stoerzinger, K. A.; Qiao, L.; Biegalski, M. D.; Shao-Horn, Y., Orientation-dependent oxygen evolution activities of rutile IrO_2 and RuO_2. *J. Phys. Chem. L* **2014,** *5* (10), 1636-1641.

[17]   Stoerzinger, K. A.; Rao, R. R.; Wang, X. R.; Hong, W. T.; Rouleau, C. M.; Shao-Horn, Y., The role of Ru redox in pH-dependent oxygen evolution on rutile ruthenium dioxide surfaces. *Chem* **2017,** *2* (5), 668-675.

[18]   Rao, R. R.; Kolb, M. J.; Halck, N. B.; Pedersen, A. F.; Mehta, A.; You, H.; Stoerzinger, K. A.; Feng, Z.; Hansen, H. A.; Zhou, H., Towards identifying the active sites on RuO_2 (110) in catalyzing oxygen evolution. *Energy Environ. Sci.* **2017,** *10* (12), 2626-2637.

[19]   Nong, H. N.; Falling, L. J.; Bergmann, A.; Klingenhof, M.; Tran, H. P.; Spöri, C.; Mom, R.; Timoshenko, J.; Zichittella, G.; Knop-Gericke, A., Key role of chemistry versus bias in electrocatalytic oxygen evolution. *Nature* **2020,** *587* (7834), 408-413.

[20]   Le Formal, F.; Pastor, E.; Tilley, S. D.; Mesa, C. A.; Pendlebury, S. R.; Grätzel, M.; Durrant, J. R., Rate law analysis of water oxidation on a hematite surface. *J. Am. Chem. Soc.* **2015,** *137* (20), 6629-6637.

[21]   Schuler, T.; Kimura, T.; Schmidt, T. J.; Büchi, F. N., Towards a generic understanding of oxygen evolution reaction kinetics in polymer electrolyte water electrolysis. *Energy Environ. Sci.* **2020,** *13* (7), 2153-2166.

[22]   Zhang, Y.; Zhang, H.; Liu, A.; Chen, C.; Song, W.; Zhao, J., Rate-limiting O–O bond formation pathways for water oxidation on hematite photoanode. *J. Am. Chem. Soc.* **2018,** *140* (9), 3264-3269.

[23]   Li, J.; Wan, W.; Triana, C. A.; Chen, H.; Zhao, Y.; Mavrokefalos, C. K.; Patzke, G. R., Reaction kinetics and interplay of two different surface states on hematite photoanodes for water oxidation. *Nat. Commun.* **2021,** *12* (1), 1-9.

[24]   Kafizas, A.; Ma, Y.; Pastor, E.; Pendlebury, S. R.; Mesa, C.; Francàs, L.; Le Formal, F.; Noor, N.; Ling, M.; Sotelo-Vazquez, C., Water oxidation kinetics of accumulated holes on the surface of a TiO2 photoanode: a rate law analysis. *ACS Catal.* **2017,** *7* (7), 4896-4903.

[25]   Mesa, C. A.; Rao, R. R.; Francàs, L.; Corby, S.; Durrant, J. R., Reply to: Questioning the rate law in the analysis of water oxidation catalysis on haematite photoanodes. *Nat. Chem.* **2020,** *12* (12), 1099-1101.

[26]   Shan, J.; Ye, C.; Chen, S.; Sun, T.; Jiao, Y.; Liu, L.; Zhu, C.; Song, L.; Han, Y.; Jaroniec, M., Short-range ordered iridium single atoms integrated into cobalt oxide spinel structure for highly efficient electrocatalytic water oxidation. *J. Am. Chem. Soc.* **2021,** *143* (13), 5201-5211.

[27]   Guan, D.; Zhou, J.; Huang, Y.-C.; Dong, C.-L.; Wang, J.-Q.; Zhou, W.; Shao, Z., Screening highly active perovskites for hydrogen-evolving reaction via unifying ionic electronegativity descriptor. *Nat. Commun.* **2019,** *10* (1), 1-8.

[28]   Guan, D.; Zhou, J.; Hu, Z.; Zhou, W.; Xu, X.; Zhong, Y.; Liu, B.; Chen, Y.; Xu, M.; Lin, H. J., Searching general sufficient-and-necessary conditions for ultrafast hydrogen-evolving electrocatalysis. *Adv. Funct. Mater.* **2019,** *29* (20), 1900704.

[29]   Cui, C.; Heggen, M.; Zabka, W.-D.; Cui, W.; Osterwalder, J.; Probst, B.; Alberto, R., Atomically dispersed hybrid nickel-iridium sites for photoelectrocatalysis. *Nat. Commun.* **2017,** *8* (1), 1-7.

[30]   Lu, Y.; Liu, T.; Dong, C. L.; Huang, Y. C.; Li, Y.; Chen, J.; Zou, Y.; Wang, S., Tuning the selective adsorption site of biomass on Co_3O_4 by Ir single atoms for electrosynthesis. *Adv. Mater.* **2021,** *33* (8), 2007056.

[31]   Dai, Y.; Yu, J.; Cheng, C.; Tan, P.; Ni, M., Engineering the interfaces in water-splitting photoelectrodes–an overview of the technique development. *J. Mater. Chem. A* **2020,** *8* (15), 6984-7002.

[32]   Sakas, G.; Ibáñez-Rioja, A.; Ruuskanen, V.; Kosonen, A.; Ahola, J.; Bergmann, O., Dynamic energy and mass balance model for an industrial alkaline water electrolyzer plant process. *Int. J. Hydrogen Energy* **2021**.

[33]   Angulo, A.; van der Linde, P.; Gardeniers, H.; Modestino, M.; Rivas, D. F., Influence of bubbles on the energy conversion efficiency of electrochemical reactors. *Joule* **2020,** *4* (3), 555-579.

[34]   Li, G.; Yang, Q.; Rao, J.; Fu, C.; Liou, S. C.; Auffermann, G.; Sun, Y.; Felser, C., In situ induction of strain in iron phosphide (FeP2) catalyst for enhanced hydroxide adsorption and water oxidation. *Adv. Funct. Mater.* **2020,** *30* (12), 1907791.

[35]   Zhu, Y.; Zhou, W.; Shao, Z., Perovskite/carbon composites: applications in oxygen electrocatalysis. *Small* **2017,** *13* (12), 1603793.

[36]   Yan, H.; Xie, Y.; Wu, A.; Cai, Z.; Wang, L.; Tian, C.; Zhang, X.; Fu, H., Anion-modulated HER and OER activities of 3D Ni–V-based interstitial compound heterojunctions

for high-efficiency and stable overall water splitting. *Adv. Mater.* **2019,** *31* (23), 1901174.

[37]   Lu, K.; Chang, G.; Zhang, H.; Yu, X.-Y., Accelerating the oxygen evolution reaction kinetics of Co_3O_4 in neutral electrolyte by decorating RuO_2. **2021,** *57* (23), 2907-2910.

[38]   Song, H. J.; Yoon, H.; Ju, B.; Kim, D. W., Highly Efficient Perovskite-Based Electrocatalysts for Water Oxidation in Acidic Environments: A Mini Review. *Adv. Energy Mater.* **2021,** *11* (27), 2002428.

[39]   Naito, T.; Shinagawa, T.; Nishimoto, T.; Takanabe, K., Recent advances in understanding oxygen evolution reaction mechanisms over iridium oxide. *Inorg, Chem. Front.* **2021**.

[40]   Long, X.; Wang, Z.; Xiao, S.; An, Y.; Yang, S., Transition metal based layered double hydroxides tailored for energy conversion and storage. *Mater. Today* **2016,** *19* (4), 213-226.

[41]   Liu, Y.; Zhu, Y.; Cui, Y., Challenges and opportunities towards fast-charging battery materials. *Nat. Energy* **2019,** *4* (7), 540-550.

[42]   Cao, P.; Zhou, X.; Wei, A.; Meng, Q.; Ye, H.; Liu, W.; Tang, J.; Yang, J., Fast-Charging and Ultrahigh-Capacity Zinc Metal Anode for High-Performance Aqueous Zinc-Ion Batteries. *Adv. Funct. Mater.* **2021,** *31* (20), 2100398.

[43]   Heidary, N.; Kornienko, N., Electrochemical biomass valorization on gold-metal oxide nanoscale heterojunctions enables investigation of both catalyst and reaction dynamics with operando surface-enhanced Raman spectroscopy. *Chem. Sci.* **2020,** *11* (7), 1798-1806.

[44]   Hopkins, B. J.; Chervin, C. N.; Parker, J. F.; Long, J. W.; Rolison, D. R., An Areal-Energy Standard to Validate Air-Breathing Electrodes for Rechargeable Zinc–Air Batteries. *Adv. Energy Mater.* **2020,** *10* (30), 2001287.